Global 3D model of mantle attenuation using seismic normal modes

Sujania Talavera-Soza (s.a.talaverasoza@uu.nl)
Utrecht University https://orcid.org/0000-0003-0947-917X
Laura Cobden
Utrecht University https://orcid.org/0000-0002-7641-9671
Ulrich Faul
MIT https://orcid.org/0000-0001-5036-4572
Arwen Deuss
Utrecht University

Physical Sciences - Article

Keywords:

Posted Date: August 2nd, 2023

DOI: https://doi.org/10.21203/rs.3.rs-1580818/v1

Additional Declarations: There is **NO** Competing Interest.

Global 3D model of mantle attenuation using seismic normal modes

Sujania Talavera-Soza[1*], Laura Cobden[1], Ulrich H. Faul[2,3], Arwen Deuss[1],

[1]Department of Earth Sciences, Utrecht University,
[2]Earth Atmospheric and Planetary Sciences, Massachusetts Institute of Technology
[3]Research School of Earth Sciences, Australian National University

*To whom correspondence should be addressed; E-mail: s.a.talaverasoza@uu.nl

Seismic tomographic models based solely on wave velocities have limited ability to distinguish between a thermal or compositional origin for Earth's 3D structure[1]. Complementing wave velocities with attenuation observations can make that distinction, which is fundamental for understanding mantle convection evolution. However, current global 3D attenuation models are only available for the upper mantle[2–4]. Here, we present a 3D global model of attenuation for the whole mantle made using whole Earth oscillations. In the upper mantle, we find high attenuation in low velocity regions, suggesting a thermal origin for spreading ridges, agreeing with previous studies[5]. In the lower mantle, we find the opposite, and observe the highest attenuation in the 'ring around the Pacific', which is seismically fast, and the lowest attenuation in the large low-seismic-velocity provinces (LLSVPs). Comparing our model to wave-speeds and attenuation predicted by a laboratory-based viscoelastic model[5] suggests that the circum-Pacific is a colder and small grain-size region, surrounding the warmer and large grain-size LLSVPs. Grain-size is proportional to viscosity in diffusion creep, implying that the LLSVPs are long-lived stable features[6].

Mantle convection is manifested at the Earth's surface through tectonic phenomena, such as volcanic eruptions and earthquakes. However, to understand the driving forces of mantle convection we need to map the physical properties of the Earth's interior. Seismic tomography has been key in unraveling Earth's internal wave-speed structure. Unfortunately, seismic tomographic models based only on wave speeds have limited ability to distinguish between a thermal or compositional origin for Earth's 3D structure variations, since temperature and bulk composition variations often change compressional and shear-wave speed with the same ratio[1]. The two most dominant features in tomographic shear-wave velocity (v_s) models are the large low-seismic-velocity provinces (LLSVPs) located in the lower mantle beneath Africa and the Pacific. The LLSVPs enfold roughly a quarter of the core-mantle boundary (CMB) region and vertically extend up to 1,200 km above the CMB[7].

The enduring question regarding these large features is if they are only thermal, i.e. their lower wave-speed is due to a higher temperature, or if they contain a different composition such as in increase in iron content[8,9]. The nature of the LLSVPs is fundamental for understanding mantle convection evolution, because a purely thermal anomaly will be short-lived[10] while compositional anomalies can form mantle 'anchors', influencing the pattern of mantle convection over long periods of time[11]. We need additional constraints to solve this question and here we show that attenuation (Q_μ^{-1}), which is the intrinsic loss of shear energy as waves travel through the Earth, may provide a new insight on the nature of the LLSVPs[5]. Attenuation is sensitive to temperature, partial melt, grain-size and, under oxidised conditions, water[12], while it remains invariant to bulk composition[13].

The few attenuation models currently available have mainly been made using surface waves. These studies focus on the upper mantle and show similarity in the upper 200 km of the mantle, where high attenuation has been found beneath spreading ridges and back-arcs, and low attenuation in shield regions[2–4,14]. Constraints on global lower-mantle attenuation have been limited to three body wave studies[15–17]. The earliest study reported a stable degree-two pattern in the lowermost mantle, with highly attenuating LLSVPs in a preliminary inversion for horizontally polarised shear-waves[15]; one of two recent studies identified a region in northeast Asia with anomalously high attenuation and a slight decrease in velocity, which was interpreted as a subducting slab transporting water into the lower mantle[16]; while the other showed that the Pacific LLSVP was on average more highly attenuating than its surrounding mantle 420 km above the CMB[17].

Studying attenuation is a challenging task, since it needs corrections for focussing and scattering, which are due to redistribution of energy and not due to intrinsic energy loss. Such corrections are difficult for body wave[15–17] and surface wave studies[2–4] and often involve approximations or extensive numerical calculations.

Normal mode observations

Here, we use whole Earth oscillations or normal modes to measure 3D variations in mantle attenuation. Normal modes allow us to include focussing and scattering without the need for approximations. This is achieved by measuring 3D variations in wave-speed and attenuation jointly, to include focussing effects, and due to the large wavelengths of the standing waves, which do not scatter off small-scale structure. We invert normal mode spectra to measure splitting functions, which are depth-averaged models of how one particular mode 'sees' the Earth. Most often only the elastic coefficients of the splitting functions are measured, which provides information on variations in wave-speed and density[18]. Here, we extend this to also include the anelastic coefficients of the splitting function[19,20], which depend on attenuation, and apply this to spheroidal modes ${}_nS_l$, where n is the overtone number and l is the angular order. Interpreting 3D mantle structure directly from splitting functions is not straightforward, given that they are integrated depth averages which need to be analysed together with their depth sensitivity kernels. However, splitting functions can give us a hint of what we can expect in a 3D model.

For example, our elastic splitting function of upper-mantle mode ${}_2S_{12}$ shows negative frequency anomalies along mid-oceanic spreading ridges (Fig. 1a). This is in agreement with predictions from mantle velocity model SP12RTS[21], and suggests that negative frequency anomalies in ridges are mainly due to low velocity (Fig. 1b). Conversely, our anelastic splitting function shows positive frequency anomalies, or high attenuation, along ridges (Fig. 1c), in agreement with upper-mantle 3D attenuation model QRFSI12[3] (Fig. 1d).

Meanwhile, the elastic splitting function of lower-mantle mode ${}_1S_9$ shows negative frequency anomalies in the areas associated with the LLSVPs, which in turn are surrounded by positive frequency anomalies (Fig. 2a). The latter is the characteristic 'ring around the Pacific' structure which dominates lower mantle

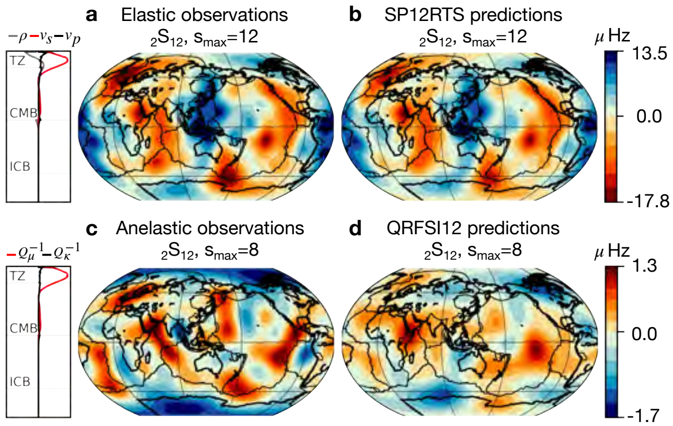

Figure 1: **Splitting function maps for upper-mantle mode $_2$S$_{12}$.** The splitting functions are plotted up to their maximum structural degree s_{max}, together with its sensitivity kernels for v_s and Q_μ^{-1} (red lines), v_p and Q_κ^{-1} (black lines) and ρ (grey line). (a) Elastic measurements compared to (b) the elastic predictions for velocity mantle model SP12RTS[21] together with crustal model CRUST5.1; and (c) anelastic measurements compared to (d) the anelastic predictions for the upper-mantle model QRFSI12[3]. Tectonic plate boundaries are included for comparison.

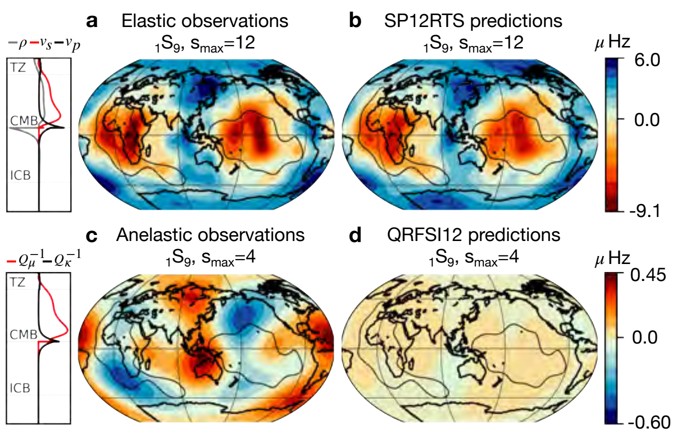

Figure 2: **Splitting function maps for lower-mantle mode $_1$S$_9$.** The -0.1% v_s outline of the tomographic model SP12RTS[21] at 2,850 km, which contours the LLSVPs, is included for comparison. See the caption of Fig. 1 for explanation.

elastic seismic structure and is also shown by SP12RTS (Fig. 2b). In contrast to the upper mantle, the anelastic splitting function shows negative frequency (low attenuation) anomalies in regions associated with low-velocity, i.e. the LLSVPs, and positive anomalies (high attenuation) in regions associated with high-velocity, i.e. the 'ring around the Pacific' (Fig. 2c).

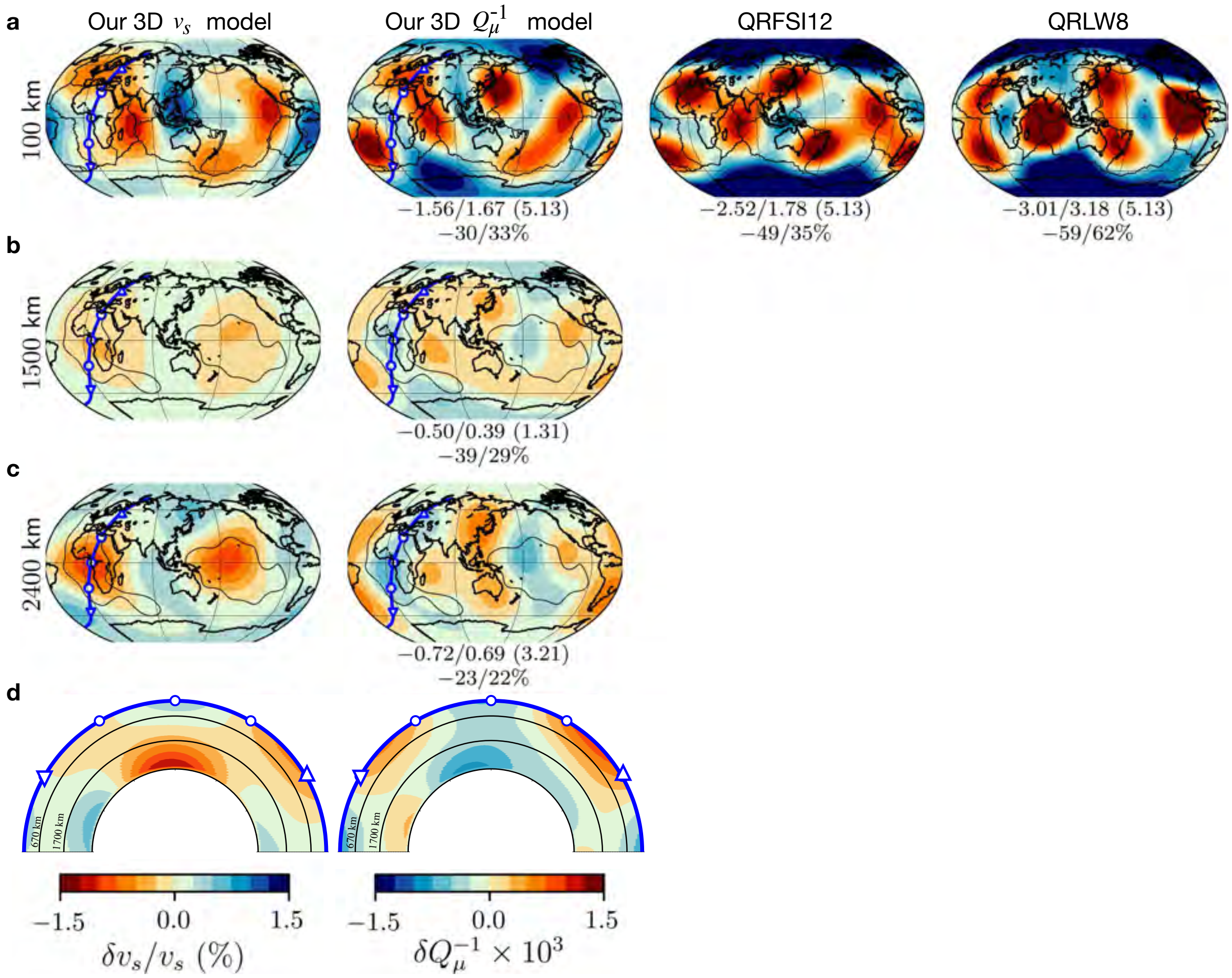

Figure 3: **Comparison between our 3D v_s model and 3D Q_μ^{-1} model**. For the upper mantle (a), the tectonic plate boundaries and the 3D upper mantle attenuation models QRLW8[2] and QRFSI12[3] are plotted. For the mid and lower mantle (b, c), the -0.1% v_s outline of the LLSVPs for tomographic model SP12RTS[21] at 2,850 km is included. A whole mantle cross-section for Africa (d) is shown for our 3D v_s and 3D Q_μ^{-1} model. All models are plotted using even-degree structure for $s = 2, 4$. Our v_s model is plotted in percentage, and all attenuation models are plotted in terms of $\delta Q_\mu^{-1} \times 10^3$, which is presented as perturbation value and in percentage (with respect to PREM), together with the peak-to-peak value at each depth.

3D mantle attenuation model

Normal mode splitting functions are linearly dependent on heterogeneous structure and can be easily incorporated into a tomographic model. We measured 14 anelastic splitting functions (${}_0S_5$-${}_0S_7$, ${}_1S_4$-${}_1S_{10}$, ${}_2S_4$-${}_2S_6$, ${}_2S_{12}$, ${}_2S_{13}$ and ${}_3S_9$ in Extended Data Figs. 1-2) and use those to built a 3D global model of attenuation (Q_μ^{-1}) for the whole mantle. The model has even spherical harmonic degrees up to degree-four structure and three b-splines for the depth parametrization (Extended Data Fig. 3a). For comparison purposes, we have also constructed a 3D shear-velocity (v_s) model using the same spheroidal modes and model parametrization.

In the upper mantle, the model shows high attenuation in the low velocity spreading ridges (Fig. 3a), agreeing with previous upper mantle models[2,3] and confirming what we already saw in the upper-mantle sensitive splitting functions (Fig. 1). In back-arc regions, the models show high attenuation and high velocities instead. However, because of the known large lateral and depth velocity variations in these areas, higher spatial resolution is needed to further interpret this behaviour. In the mid and lower mantle, our 3D Q_μ^{-1} model shows the highest attenuation in the circum-Pacific region (Fig. 3b-c), which is thought to be the 'graveyard' of subducted slabs, and not in the LLSVPs. Just like previous models, the v_s structure in our model has a dominant degree-two signal, which is still visible even when including larger structural degrees. Our 3D Q_μ^{-1} model, on the other hand, shows more regional variations than v_s. As a consequence, in the 3D Q_μ^{-1} model, parts of the LLSVPs have low attenuation, but some other parts, especially the edges, have higher attenuation.

Because the correlation between 3D v_s and 3D Q_μ^{-1} changes in our model from the upper to the lower mantle, we performed a number of synthetic tests and found that this change in behaviour is indeed required by the data and can be recovered in our synthetic modelling (see Method and Extended Data Fig. 7d-e). We also tested if we would be able to recover the presence of a distinct $\sim$400 km layer located at the bottom of the lower mantle, which was not possible (Extended Data Fig. 7d-e). This implies that with our current dataset and parametrization we cannot resolve fine-scale attenuation structure in the lowermost mantle, especially when this structure differs from the rest of the lower mantle. This might be the reason our model differs from previous body wave attenuation studies, which are dominantly sensitive to the lowermost mantle[15–17].

Mineral physics interpretation

To understand the physical origin of the structures in our seismic model, we compare our results with the wave-speeds and attenuation predicted by the laboratory-based viscoelastic 'Extended Burgers Model' (EBM)[5]. The EBM provides v_s and Q_μ^{-1} predictions as a function of grain-size and temperature for a given

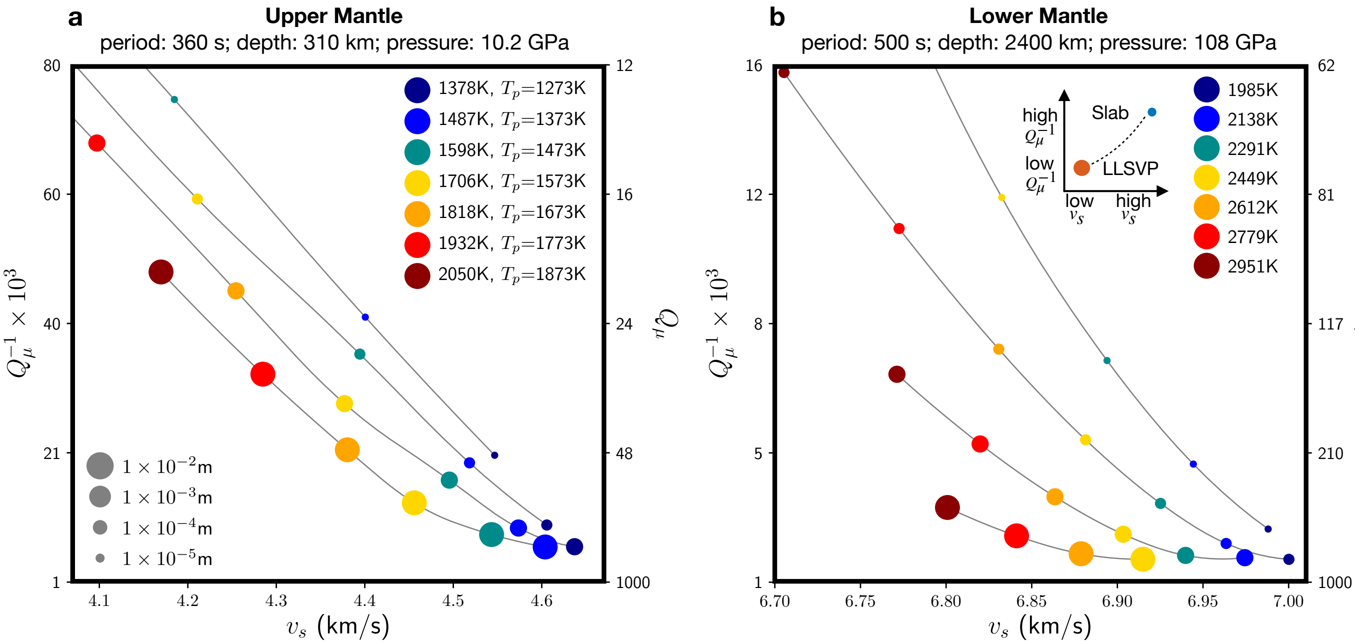

Figure 4: **Relationship between v_s and Q_μ^{-1}.** Modelling performed with the EBM[5] by varying temperature T (K) and grain-size d (m) and the parameters listed in Extended Data Table 2. The potential temperature T_p associated to each T and its corresponding adiabat is listed. The upper mantle behaviour (a) is shown at 2.7 mHz and 310 km, and the lower mantle (b) is shown at 2 mHz and 2,400 km. The inset figure in (B) shows an schematic describing the expected behaviour between LLSVPs and slabs.

period and depth in the Earth's mantle (Fig. 4). These predictions were calculated using previously constrained thermodynamic and rheological parameters (see Methods and Extended Data Table 2), and show that increasing temperature or decreasing grain-size lowers v_s and increases attenuation[5]. In the upper mantle, our models shows high attenuation and low velocities in ridges, and low attenuation and high velocity in cratons (Figs. 3a, 3d). Thus, our attenuation model indicates that upper-mantle large scale anomalies have a predominantly thermal origin (Fig. 4a).

There is limited information on anelastic properties of lower-mantle minerals. Experimental attenuation studies on MgO[22,23] and perovskite analogues at low pressure[24] find that they show similar frequency, temperature and grain-size sensitivity as olivine. This means that an increase in temperature or the presence of partial melt[25,26] are expected to lead to low velocity in combination with high attenuation[5], which is not what we observe.

Deeper in the lower mantle, bridgmanite may transform to post-perovskite[27,28]. Estimates of the depth range of this phase transition have large uncertainties, varying between $\sim$440 km (113 GPa) above the CMB and $\sim$80 km (144 GPa) below the CMB[29]. Post-perovskite is most likely present in colder areas and has been shown to be potentially highly attenuating[30]. However, we cannot resolve the bottom 400 km of the lower mantle with confidence (Extended Data Fig. 7d-e), which means the presence of post-perovskite is also unlikely to explain our observations. This implies that the LLSVPs require variations in another physical property.

Comparing our 3D attenuation model to the wave-speeds and attenuation predicted by the EBM shows that variations in both grain size and temperature are very consistent with our lower mantle attenuation observations. Subducting slabs are expected to reset their grain-size in the transition zone due to the phase transformation across the 660 km discontinuity[31], with little grain growth at the cold temperatures of slabs in the lower mantle[6]. Thus, the higher attenuation seen in the slab regions can be explained by a small grain-size in combination with cold temperatures, while the lower attenuation in the LLSVPs can be explained by a large grain-size in combination with high temperatures (Fig. 4b). This is reasonable since, kinetically, higher temperatures lead to faster grain-growth rates and larger grain-sizes[31]. For example, the EBM (Fig. 4b) shows that a hotter temperature (2,779 K) and coarser-grain-size (1×10^{-2} m) makes the LLSVPs less attenuating ($Q_\mu^{-1} \times 10^3 \sim 2.3$) and slower ($v_s \sim 6.84$ km/s), than a relatively colder (2,291 K) and finer-grained (1×10^{-5} m) slab ($Q_\mu^{-1} \times 10^3 \sim 7.7$, $v_s \sim 6.9$ km/s). Following this assumption, the EBM predicts lateral variations in grain-size from one up to three orders of magnitude, together with temperature differences of 450-500 K between the LLSVPs and the circum-Pacific. The former agrees with previous numerical modelling studies[6,32], which suggest that grain sizes may vary laterally by one order[6] or two orders[32] of magnitude in the lower mantle. The temperature differences agree with Deschamps et al.[33], who inferred that the LLSVPs require an increase in temperature of 400-700 K (Fig. 4b).

Geodynamical implications

Our 3D mantle attenuation model and its physical interpretation are consistent with geodynamical models arguing that cold slabs are expected to have small grain sizes in the lower mantle, while hot LLSVPs could potentially be large grain-size provinces[6]. This comes as a result of grain sizes in the lower mantle being controlled by the residence time and temperature of the material[6]. Grain size is related to viscosity in diffusion creep, which would mean that the larger grain LLSVPs have larger viscosity making them long-lived stable features[11], while the 'graveyard' of slabs would have a lower viscosity making them shorter lived. Furthermore, if the grain size is large enough for dislocation creep to occur, the calculated viscosity would likely be even higher[34]. This idea is further reinforced by recent laboratory experiments, which show that grain growth at lower mantle conditions is indeed significantly faster than previously predicted[31]. At topmost lower mantle conditions (2,000 K, 27 GPa), the ambient mantle will take 1 Gyr to reach a grain size of $\sim 1 \times 10^{-4}$ m, while subducted slabs will have grains an order of magnitude smaller[31]. This means hotter material in the LLSVPs would have a faster growth rate together with an inferred long residence time in the lower mantle, leading to a significantly larger grain size. Our findings are also consistent with the prediction that LLSVPs are enriched in bridgmanite[23,33], which would be less attenuating. At the same time, bridgmanite enrichment results in faster grain growth with respect to the surrounding slabs relatively enriched in ferropericlase, even when at the same temperature and residence time.

Recently, bridgmanite-enriched ancient mantle structures (BEAMS)[35] have been proposed as an alternative hypothesis to explain the driving forces of mantle convection. In geodynamics models, BEAMS manifest in the mid mantle (1,000-2,000 km) and may overlay the LLSVPs and constrain their shape[36]. So far, BEAMS have not been directly observed in tomographic models. However, they are also consistent with large grain-sizes and a long residence time in the lower mantle. This mean that alternatively, the large size of the BEAMs could dominate the lower mantle signal of our 3D attenuation model and be the source of the low attenuation above the LLSVPs.

Overall, whether the LLSVPs or BEAMS are the main source of the low attenuation, having LLSVPs that are coarse grained regions, with consequent high viscosity[6], is a prerequisite for their stability and longevity, which can be further stabilized by a dense chemical component at the base of the lower mantle[7–9].

Acknowledgments

S.T.S. and A.D. received funding from the European Research Council (ERC) under the European Union's Horizon 2020 research and innovation programme (grant agreement No. 681535 - ATUNE) and a Vici award number 016.160.310/526 from the Dutch Research Council (NWO). L.C. received funding from a Vidi award number 016.Vidi.171.022 from the NWO.

Author contributions

S.T.S. designed and performed the seismic observations and tests, built and validated the 3D models, and lead the interpretation of the results. L.C. and U.H.F. contributed to the mineral physics analysis and interpretation of the results. U.H.F. developed the software used to calculate the mineral physics predictions. L.C. and S.T.S. wrote the computing infrastructure used to calculate the mineral physics predictions. A.D. and S.T.S. wrote the software and computing infrastructure used to do the seismic observations and models. A.D. conceived the idea of the project and contributed to the development of the observations and models, as well as the interpretation of the results. S.T.S. developed the supplementary information and wrote the manuscript, following discussions with and contributions from all authors.

Author information

The authors declare no competing interests. Correspondence and requests for materials should be addressed to S.T.S. (s.a.talaverasoza@uu.nl).

References

1. Deschamps, F. & Trampert, J. Mantle tomography and its relation to temperature and composition. *Phys. Earth Planet. Inter.* **140**, 277–291 (2003).

2. Romanowicz, B. & Gung, Y. Superplumes from the core-mantle boundary to the lithosphere: Implications for heat flux. *Science* **296**, 513–516 (2002).

3. Dalton, C. A., Ekström, G. & Dziewonski, A. M. The global attenuation structure of the upper mantle. *J. Geophys. Res. Solid Earth* **113** (2008).

4. Karaoğlu, H. & Romanowicz, B. Inferring global upper-mantle shear attenuation structure by waveform tomography using the spectral element method. *Geophys. J. Int.* **213**, 1536–1558 (2018).

5. Faul, U. H. & Jackson, I. Transient creep and strain energy dissipation: An experimental perspective. *Annu. Rev. Earth Planet. Sci.* **43**, 541–569 (2015).

6. Dannberg, J. *et al.* The importance of grain-size to mantle dynamics and seismological observations. *Geochem. Geophys. Geosyst.* **18**, 3034–3061 (2017).

7. Garnero, E. J., McNamara, A. K. & Shim, S.-H. Continent-sized anomalous zones with low seismic velocity at the base of Earth's mantle. *Nat. Geosci.* **9**, 481–489 (2016).

8. Trampert, J., Deschamps, F., Resovsky, J. & Yuen, D. Probabilistic tomography maps chemical heterogeneities throughout the lower mantle. *Science* **306**, 853–856 (2004).

9. Lau, H. C. P. *et al.* Tidal tomography constrains Earth's deep-mantle buoyancy. *Nature* **551**, 321 (2017).

10. Zhang, N., Zhong, S., Leng, W. & Li, Z.-X. A model for the evolution of the Earth's mantle structure since the early Paleozoic. *J. Geophys. Res. Solid Earth* **115** (2010).

11. Torsvik, T. H. *et al.* Deep mantle structure as a reference frame for movements in and on the Earth. *Proc. Natl. Acad. Sci.* **111**, 8735–8740 (2014).

12. Cline II, C. J., Faul, U. H., David, E. C., Berry, A. J. & Jackson, I. Redox-influenced seismic properties of upper-mantle olivine. *Nature* **555**, 355–358 (2018).

13. Qu, T., Jackson, I. & Faul, U. H. Low-frequency seismic properties of olivine-orthopyroxene mixtures. *J. Geophys. Res. Solid Earth* **126**, e2021JB022504 (2021).

14. Zhu, H., Bozdağ, E., Duffy, T. S. & Tromp, J. Seismic attenuation beneath Europe and the North Atlantic: Implications for water in the mantle. *Earth Planet. Sci. Lett.* **381**, 1–11 (2013).

15. Romanowicz, B. Attenuation tomography of the Earth's mantle: a review of current status. *Pure Appl. Geophys.* **153**, 257–272 (1998).

16. Lawrence, J. F. & Wysession, M. E. Seismic evidence for subduction-transported water in the lower mantle. *Geophys. Monogr. AGU* **168**, 251 (2006).

17. Hwang, Y. K. & Ritsema, J. Radial Q_μ structure of the lower mantle from teleseismic body-wave spectra. *Earth Planet. Sci. Lett.* **303**, 369–375 (2011).

18. Deuss, A., Ritsema, J. & van Heijst, H. J. A new catalogue of normal-mode splitting function measurements up to 10 mHz. *Geophys. J. Int.* **193**, 920–937 (2013).

19. Masters, G., Laske, G. & Gilbert, F. Autoregressive estimation of the splitting matrix of free-oscillation multiplets. *Geophys. J. Int.* **141**, 25–42 (2000).

20. Mäkinen, A. M. & Deuss, A. Normal mode splitting function measurements of anelasticity and attenuation in the Earth's inner core. *Geophys. J. Int.* **194**, 401–416 (2013).

21. Koelemeijer, P., Ritsema, J., Deuss, A. & van Heijst, H. J. SP12RTS: A degree-12 model of shear-and compressional-wave velocity for Earth's mantle. *Geophys. J. Int.* **204**, 1024–1039 (2016).

22. Webb, S. & Jackson, I. Anelasticity and microcreep in polycrystalline MgO at high temperature: An exploratory study. *Phys. Chem. Miner.* **30**, 157–166 (2003).

23. Barnhoorn, A., Jackson, I., Fitz Gerald, J., Kishimoto, A. & Itatani, K. Grain size-sensitive viscoelastic relaxation and seismic properties of polycrystalline MgO. *J. Geophys. Res. Solid Earth* **121**, 4955–4976 (2016).

24. Webb, S., Jackson, I. & Gerald, J. F. Viscoelasticity of the titanate perovskites $CaTiO_3$ and $SrTiO_3$ at high temperature. *Phys. Earth Planet. Inter.* **115**, 259–291 (1999).

25. Jackson, I., Faul, U. H., Fitz Gerald, J. D. & Tan, B. H. Shear wave attenuation and dispersion in melt-bearing olivine polycrystals: 1. Specimen fabrication and mechanical testing. *J. Geophys. Res. Solid Earth* **109** (2004).

26. McCarthy, C. & Takei, Y. Anelasticity and viscosity of partially molten rock analogue: Toward seismic detection of small quantities of melt. *Geophys. Res. Lett.* **38** (2011).

27. Murakami, M., Hirose, K., Kawamura, K., Sata, N. & Ohishi, Y. Post-perovskite phase transition in $MgSiO_3$. *Science* **304**, 855–858 (2004).

28. Oganov, A. R. & Ono, S. Theoretical and experimental evidence for a post-perovskite phase of $MgSiO_3$ in Earth's D" layer. *Nature* **430**, 445–448 (2004).

29. Cobden, L., Thomas, C. & Trampert, J. Seismic detection of post-perovskite inside the Earth. In *The Earth's heterogeneous mantle*, 391–440 (Springer, 2015).

30. Goryaeva, A. M., Carrez, P. & Cordier, P. Low viscosity and high attenuation in $MgSiO_3$ post-perovskite inferred from atomic-scale calculations. *Sci. Rep.* **6**, 34771 (2016).

31. Fei, H., Faul, U. H. & Katsura, T. The grain growth kinetics of bridgmanite at the topmost lower mantle. *Earth Planet. Sci. Lett.* **561**, 116820 (2021).

32. Glišović, P., Forte, A. M. & Ammann, M. W. Variations in grain size and viscosity based on vacancy diffusion in minerals, seismic tomography, and geodynamically inferred mantle rheology. *Geophys. Res. Lett.* **42**, 6278–6286 (2015).

33. Deschamps, F., Cobden, L. & Tackley, P. J. The primitive nature of large low shear-wave velocity provinces. *Earth Planet. Sci. Lett.* **349**, 198–208 (2012).

34. Boioli, F. *et al.* Pure climb creep mechanism drives flow in Earth's lower mantle. *Sci. Adv.* **3**, e1601958 (2017).

35. Ballmer, M. D., Houser, C., Hernlund, J. W., Wentzcovitch, R. M. & Hirose, K. Persistence of strong silica-enriched domains in the Earth's lower mantle. *Nat. Geosci.* **10**, 236–240 (2017).

36. Gülcher, A. J. P., Ballmer, M. D. & Tackley, P. J. Coupled dynamics and evolution of primordial and recycled heterogeneity in Earth's lower mantle. *Solid Earth* **12**, 2087–2107 (2021).

Methods

Normal Modes

Normal modes are standing waves along the surface and the radius of a planet. We focus on measuring spheroidal modes ${}_nS_l$, which involve P-SV wave motion, where n is the overtone number and l is the angular order. Modes with $n = 0$ are called fundamentals, and modes with $n > 0$ are called overtones. Each normal mode is a multiplet consisting of $2l + 1$ singlets. In a spherical, non-rotating, elastic, isotropic Earth the $2l + 1$ singlets are degenerate, meaning they all have the same frequency ω_0. This degeneracy is removed by the effects of rotation, ellipticity, anisotropy and lateral heterogeneities, which we call splitting. We calculate splitting through perturbation theory[37–39]. Here, we do this calculation using the self-coupling approximation, where modes are treated as isolated; and the group-coupling approximation, which includes the cross-coupling or resonance between two or more modes close in frequency, which is used to measured two mode pairs (i.e. ${}_1S_5$-${}_2S_4$, ${}_1S_6$-${}_2S_5$).

Splitting functions

Splitting functions fully describe the splitting of modes due to lateral heterogeneity in velocity, density and attenuation. In general, for a given mode, the complex splitting function coefficients σ_{st} are defined as

$$\sigma_{st} = c_{st} + \mathrm{i}d_{st} \tag{1}$$

where s is the angular order and t the azimuthal order of the Earth's structure. The real part c_{st} describes the elastic structure, depending linearly on heterogeneous velocity and density structure. The elastic splitting function coefficients c_{st} are written as

$$c_{st} = \int_0^a \delta m_{st}(r) \cdot K_s(r)\,\mathrm{d}r + \sum_d \delta h^d_{st}\, H^d_s \tag{2}$$

where the integral is calculated over a, the radius of the Earth. $K_s(r)$ and H^d_s are known kernels[39]; δm_{st} are the coefficients of the Earth's structure (compressional and shear wave velocity v_p, v_s, which can be anisotropic, and density ρ) and δh^d_{st} are the coefficients of discontinuity topography.

The imaginary part d_{st} describes the anelastic structure, depending linearly on heterogeneous bulk and shear attenuation. The anelastic splitting function coefficients d_{st} are written as

$$d_{st} = \frac{1}{2}\omega_0^{-2} \int_0^a \left(\mu_0 \, \delta Q^{-1}_{\mu(st)} \, K_s^{Q_\mu^{-1}}(r) + \kappa_0 \, \delta Q^{-1}_{\kappa(st)} \, K_s^{Q_\kappa^{-1}(kk')}(r) \right) r^2 \mathrm{d}r \tag{3}$$

where $K_s^{Q_\mu^{-1}}(r)$ is again a known kernel[39]; $\delta Q^{-1}_{\mu(st)}$ are the shear attenuation structure coefficients; and μ is the shear modulus (rigidity). Here, we consider 3D bulk (incompressibility) attenuation structure negligible.

Splitting functions are depth-averaged models of how one particular mode ‘sees’ the Earth. They show where locally the frequency of a mode is slightly higher or lower than its center frequency[40]. They can be visualised in a map $F(\theta, \phi)$, comparable to phase-velocity maps used in surface wave analysis

$$F(\theta, \phi) = \sum_{s=2}^{2l} \sum_{t=-s}^{s} Y_s^t(\theta, \phi) \, \sigma_{st} \tag{4}$$

The splitting function coefficients are used to calculate the splitting matrix, which together with the effects of the 1D reference model[41], ellipticity and rotation allow us to calculate synthetic spectra. These synthetic spectra are then used to measure splitting functions from the spectra of real large earthquakes[18]. Because of the non-linear dependence of the synthetic seismograms on c_{st} and d_{st}, this process is iterative, which means that we need to calculate the derivatives of the synthetic spectra with respect to c_{st} and d_{st} in each iteration. To perform this inversion, we use use the damped iterated least-squares method[42], which in combination with the forward problem setup described is referred to in the literature as iterative spectral fitting[43]. Here, we follow the same methodology and misfit calculation as previous work[18,20].

Seismic data

We use a previously published earthquake catalogue[18], and added 14 additional large earthquakes that occurred between 2012 and 2018[44]. Horizontal component data was also added to the catalogue[45], which previously only contained vertical component data. The extended catalogue now consists of 107 earthquakes with magnitude $M_w > 7.4$ which occurred in the period from 1975 to 2018, providing us with an average increase of 24% in the number of spectra per mode. The 2004 Sumatra earthquake was excluded from our measurements and tests given its complicated source and associated uncertainties.

Elastic and anelastic splitting function measurements

Based on the relationship between 3D attenuation upper-mantle model QRFSI12[3] and 3D v_s mantle model S20RTS[46], we expect that the anelastic splitting function coefficients d_{st} measured from real data will be on average around 10 times smaller than the elastic splitting function coefficients c_{st}[44]. Because of this, we first measure the larger c_{st} coefficients on their own and apply the same damping to all coefficients. In the second step of the measurement process, we use these c_{st} measurements as our starting model, and then measure c_{st} and d_{st} coefficients simultaneously, while starting all d_{st} measurements from PREM[41], and again apply the same damping to all coefficients. This approach was tested using synthetic data, where we confirmed that, even in the synthetic case, the d_{st} coefficients can only be recovered when the c_{st} coefficients were measured first and later used as a starting model in a joint c_{st} and d_{st} inversion. We select the optimal damping value by evaluating the misfit, the squared model size and the effective number of independent model parameters as a function of iteration and damping.

Furthermore, to avoid aliasing, all c_{st} measurements for a given mode ${}_nS_l$ were done up to their highest possible structural degree ($s_{max} = 2l$). The d_{st} coefficients of modes with $2l \leq 12$ were also measured up to their highest possible structural degree ($s_{max} = 2l$). However, modes with $2l > 12$ were measured to a lower structural degree ($s_{max} = 12$). For these modes not enough data is available to measure both c_{st} and d_{st} coefficients up to their highest structural degree. For example, the c_{st} coefficients of mode ${}_2S_{12}$ were measured up to $s_{max} = 24$, while its d_{st} coefficients were measured up to $s_{max} = 12$. Mode pairs ${}_1S_6$-${}_2S_5$ and ${}_1S_5$-${}_2S_4$ were measured in group-coupling using the same frequency window for both modes. For these modes, the self-coupling splitting functions are measured using the same procedure described above. The elastic cross-coupling was measured up to its highest possible structural degree, while the anelastic cross-coupling was not measured.

We measured anelastic splitting function coefficients for 12 spheroidal modes in self-coupling, and two spheroidal mode pairs in group-coupling (Extended Data Table 1 and Fig. 1). All the elastic splitting functions are dominated by v_s mantle sensitivity, while the anelastic functions are dominated by Q_μ^{-1} mantle sensitivity (Extended Data Fig. 2). When comparing the misfit of our 3D elastic measurement inversion to the misfit of our combined 3D elastic and anelastic inversion (Extended Data Table 1), we find a statistically significant but relatively small misfit reduction ($\sim$3%) when the anelastic splitting function is included compared to only including the elastic spitting function. This is especially evident when comparing our results to the larger misfit reductions ($\sim$13%) found in similar measurements for inner core sensitive modes[20]. However, we argue that the reason for our low misfit reduction, when compared to similar measurements of inner core sensitive modes, is that 3D anelasticity has a much stronger effect on inner core sensitive modes than on mantle sensitive modes[44].

Model predictions

We compare our measured splitting functions to predictions computed for existing tomographic models. For the elastic case, we use the compressional and shear wave velocity model SP12RTS[21], with a scaling of the form $\delta\rho/\rho = 0.3\,\delta v_s/v_s$; and the shear wave velocity model S20RTS[46], with a scaling of the form $\delta v_p/v_p = 0.5\,\delta v_s/v_s$ and $\delta\rho/\rho = 0.3\,\delta v_s/v_s$. We perform elastic crustal corrections using model CRUST5.1[47]. For the anelastic case, we use the upper-mantle 3D shear attenuation models QRLW8[2] and QRFSI12[3].

To perform robustness tests, we use a synthetic global 3D Q_μ^{-1} mantle model, by applying the scaling $\delta Q_\mu^{-1} = R_q\,\delta v_s/v_s$ to the 3D v_s model S20RTS[44]. We use $R_q = -0.2$, which we calculated based on the average relationship between the 3D Q_μ^{-1} variations in model QRFSI12 and the 3D v_s variations in models S20RTS, S362ANI+M[48], and SEMum2[49]. In our synthetic tests, this R_q value was later extrapolated either to the whole mantle, generating a 3D Q_μ^{-1} synthetic model completely anti-correlated to v_s, or its absolute value was extrapolated with different polarities in the upper or lower mantle, e.g. $R_q = -0.2$ for 24-670 km, $R_q = +0.2$ for 670-2,491 km and $R_q = -0.2$ for 2,491-2,891 km. In all tests, we were able to recover the input synthetic structure (see Supplementary Information).

3D attenuation model

Elastic splitting functions are linearly dependent on heterogeneous velocity structure, while anelastic splitting functions are linearly dependent on heterogeneous attenuation structure (Eqs. 2-3). This linear dependence means splitting functions can be easily incorporated in tomographic modelling inversions[21,46,48,50]. We take advantage of this, and create global tomographic models of 3D shear velocity and 3D shear attenuation using our elastic and anelastic splitting function observations respectively (Extended Data Table 1) in a damped least squares inversion[42].

Parametrization

We use cubic b-splines radially[51] (Extended Data Fig. 3a) and spherical harmonics coefficients laterally[21,46] to parameterize our mantle models. We also experimented with an alternative radial parametrization using boxcars to further confirm our model results (Extended Data Fig. 3b). Because of the limited amount of mantle anelastic splitting function observations (Extended Data Table 1), we apply a coarse depth and spherical harmonic parametrization. We use 3 b-splines or 3 boxcars radially, and we invert our model only for even degree spherical harmonics up to degree four.

In order to evaluate our depth parametrization, we performed inversions using both a b-spline and boxcar parametrizations. Both of them yielded similar results, however the b-spline depth parametrization provided lower misfits and smoother models, and here we present only our models results using this parametrization.

Crustal corrections

Before the model inversion, we do crustal corrections to our elastic splitting function observations using crustal model CRUST5.1[47]. But, we do not perform anelastic crustal corrections on our anelastic splitting function observations. However, based on the previous analysis[4,52], we do not expect the anelastic crustal corrections to significantly affect our final 3D Q_{μ}^{-1} model. In addition, the observed upper-mantle modes do not have their peak sensitivities at crustal depths.

Inversion method, weighting and model predictions

To obtain the models we calculate the derivatives of our elastic splitting function coefficients c_{st} with respect to the elastic structure model parameters m_{st} ($\delta v_s/v_s$ in our case), and the derivatives of our anelastic splitting function coefficients d_{st} with respect to the shear attenuation structure model parameters $Q^{-1}_{\mu(st)}$. Because this is a linear problem, this process is not iterative and the partial derivatives are the same as the kernels in Eqs. 2-3:

$$\frac{\partial c_{st}}{\partial m_{st}} = K_s^{v_s}(r) \tag{5}$$

$$\frac{\partial d_{st}}{\partial Q^{-1}_{\mu(st)}} = \frac{\mu_0}{2\omega_0} K_s^{Q_\mu^{-1}}(r) \tag{6}$$

We follow the same methodology, weighting strategy (by the coefficient uncertainties) and misfit of the second step of the two-step inversion of a previous study[53], which again uses the damped iterated least-squares method[42] to solve the inverse problem. We also performed inversions with un-weighted coefficients that provided similar models, but with higher misfits to the observations.

By analysing the sensitivity kernels of our observed modes, we consider the mid mantle ($\sim$ 670-1,900 km) to be the least constrained region in our anelastic measurements[44]. For this reason, we apply an order of magnitude higher damping in the mid-mantle spline than in the upper or lower-mantle splines (Extended Data Fig. 3a). We also performed inversions where the same damping was applied to all splines. These inversions again provided similar models, but with higher misfits to the observations.

To select the best model, we analyse the L-curve of the models resulting from a large range of damping parameters, which shows the variance reduction (misfit) against the model size ($\sum_{s=0}^{s_{max}} \sum_{t=-s}^{s} m_{st}^2$) (Extended Data Fig. 4a). In order to maximize the variance reduction and minimize the model size, while avoiding filling the null space of the model, the selected optimum damping for our final model lies near the 'kink' of the L-curve (Extended Data Fig. 4a).

To further investigate the fit of the 3D Q_μ^{-1} model to the input data, we compare our measured anelastic splitting function observations to the predictions of our final attenuation model. We find that our 3D Q_μ^{-1} model indeed sufficiently predicts all of our anelastic splitting function coefficients (Extended Data Fig. 5).

Sensitivity and long-wavelength structure

The data sensitivity for the k^{th} spline of the model is defined using a horizontal average[21,53,54]. The model sensitivity is dominated by our upper-mantle modes, however we still have significant sensitivity for the lower mantle (Extended Data Fig. 4b). We also analized the long-wavelength spectral content of our 3D Q_μ^{-1} and v_s models (Extended Data Fig. 6). These results show that degree-two structure dominates both the upper and lower mantle structure of our model, while degree-four structure has greater spectral content in the upper mantle.

Synthetic tests

We used a synthetic model to test the spatial resolution of our 3D Q_μ^{-1} model in the lower mantle. The synthetic model contained the same change in behaviour in mantle attenuation at the transition zone that we see in our real model, meaning we set $R_q = -0.2$ from 24-670 km and $R_q = +0.2$ from 670-2,491 km. We were able to recover this change in correlation at the transition zone using our method (Extended Data Fig. 7a-c). The model also contained a distinct layer located at the bottom $\sim$400 km of the mantle ($R_q = -0.2$ from 2,491-2,891 km), which we were unable to recover (Extended Data Fig. 7d-e). This implies that with our current data-set and parametrization we cannot retrieve attenuation structure in the lowermost mantle when this structure differs from the rest of the lower mantle.

Although we are not able to recover a thin distinct layer at the bottom of the lower mantle, we do measure its influence in the recovered model. The recovered LLSVP structure experiences a shift with respect to the input, and also begins to split into two separate blobs (Extended Data Fig. 7c-d). This comes as a consequence of the distinct layer introduced in the synthetic model, and we observe a similar behaviour in our 3D Q_μ^{-1} model (Extended Data Fig. 7d). This may explain why our model differs from previous attenuation studies based on body waves[15–17], who observed high attenuation in the lowermost mantle, i.e. that our model has both a low depth resolution and low sensitivity to thin attenuation structures in the D” region.

Extended Burgers Model (EBM)

In order to model the behaviour of attenuation of mantle minerals as a result of different mechanisms and as a function of temperature, grain-size and seismic period, we use the Extended Burgers Model (EBM)[5,55]. The EBM, which incorporates the instantaneous elastic response, two different types of anelastic behaviour, and Newtonian viscous deformation, was constructed by fitting experimental data for polycrystalline olivine using a large range of grain sizes (3-165 μm), high temperatures (800-1200°C) and seismic periods (1-1000 s).

The parameters used in this study are listed in Extended Data Table 2 and are based in previously reported values[6,56]. The frequency dependence of Q_μ^{-1} using Extended Data Table 2 follows the same behaviour as another recent study[56] (Extended Data Fig. 8). The elastic wave-speeds are calculated using Perple_X[57] with the equation of state and mineral elastic parameters given in previous studies[58,59] using pyrolite composition[60,61].

For the lower mantle, calculations were done at 108 GPa, which is similar to 2,400 km depth. For the upper mantle, calculations were done at 10.2 GPa, which is similar to 310 km depth. The range of temperatures plotted in Fig. 4 (1,985 to 2,851 K for the lower mantle) is based on a compilation of geotherms[62], and adiabats[63]. Pyrolite adiabats were calculated again using Perple_X, where we extract constant entropy contours for a given potential temperature[59,61].

We consider grain-sizes between 1×10^{-2} m and 1×10^{-5} m, which are based on previous numerical modelling studies[6,32]. The first study suggests that grain-sizes may vary laterally by 1 order of magnitude in the lower mantle[6], while the second suggests a difference of 2 orders of magnitude should be theoretically possible[32].

Data and materials availability

The facilities of IRIS Data Services, and specifically the IRIS Data Management Center, were used for access to waveforms, related metadata, and/or derived products used in this study. We also acknowledge the 'Global CMT project' webpage for the earthquake source parameters used in this study. The data analysis was done using ObsPy[64] and FrosPy[65]. Figures were prepared using Python[66], FrosPy[65] and Generic Mapping Tools software[67]. Supplementary Information is available for this paper.

Code availability

Computer codes used to produce the seismic observations and models will be made available upon request to A.D. (a.f.deuss@uu.nl). Computer codes used to produce the mineral physics predictions will be made available upon request to U.H.F. (hufaul@mit.edu). Mineral elastic properties were calculated using Perple_X[57] which is freely available on: https://www.perplex.ethz.ch.

Method references

37. Dahlen, F. A. The normal modes of a rotating, elliptical Earth. *Geophys. J. Int.* **16**, 329–367 (1968).

38. Woodhouse, J. H. & Dahlen, F. A. The effect of a general aspherical perturbation on the free oscillations of the Earth. *Geophys. J. Int.* **53**, 335–354 (1978).

39. Woodhouse, J. H. The coupling and attenuation of nearly resonant multiplets in the Earth's free oscillation spectrum. *Geophys. J. Int.* **61**, 261–283 (1980).

40. Woodhouse, J. H. & Giardini, D. Inversion for the splitting function of isolated low order normal mode multiplets. *Eos Trans. AGU* **66**, 300 (1985).

41. Dziewonski, A. M. & Anderson, D. L. Preliminary Reference Earth Model. *Phys. Earth Planet. Inter.* **25**, 297–356 (1981).

42. Tarantola, A. & Valette, B. Generalized nonlinear inverse problems solved using the least squares criterion. *Rev. Geophys.* **20**, 219–232 (1982).

43. Resovsky, J. & Ritzwoller, M. New and refined constraints on three-dimensional Earth structure from normal modes below 3 mHz. *J. Geophys. Res. Solid Earth* **103**, 783–810 (1998).

44. Talavera-Soza, S. *Observing seismic attenuation in the Earth's mantle and inner core using normal modes*. Ph.D. thesis, Utrecht University (2021).

45. Schneider, S. & Deuss, A. A new catalogue of toroidal-mode overtone splitting function measurements. *Geophys. J. Int.* (2020).

46. Ritsema, J., van Heijst, H. J. & Woodhouse, J. H. Complex shear wave velocity structure imaged beneath Africa and Iceland. *Science* **286**, 1925–1928 (1999).

47. Mooney, W., Laske, G. & Masters, G. CRUST5.1: A global model at 5 degrees by 5 degrees. *J. Geophys. Res* **102**, 727–748 (1998).

48. Moulik, P. & Ekström, G. An anisotropic shear velocity model of the Earth's mantle using normal modes, body waves, surface waves and long-period waveforms. *Geophys. J. Int.* **199**, 1713–1738 (2014).

49. French, S. W., Lekić, V. & Romanowicz, B. Waveform tomography reveals channeled flow at the base of the oceanic asthenosphere. *Science* **342**, 227–230 (2013).

50. Ritsema, J., Deuss, A., van Heijst, H. J. & Woodhouse, J. H. S40RTS: A degree-40 shear-velocity model for the mantle from new Rayleigh wave dispersion, teleseismic traveltime and normal-mode splitting function measurements. *Geophys. J. Int.* **184**, 1223–1236 (2011).

51. Mégnin, C. & Romanowicz, B. The three-dimensional shear velocity structure of the mantle from the inversion of body, surface and higher-mode waveforms. *Geophys. J. Int.* **143**, 709–728 (2000).

52. Dalton, C. A. & Faul, U. H. The oceanic and cratonic upper mantle: Clues from joint interpretation of global velocity and attenuation models. *Lithos* **120**, 160–172 (2010).

53. Jagt, L. & Deuss, A. Comparing one-step full-spectrum inversion with two-step splitting function inversion in normal mode tomography. *Geophys. J. Int.* **227**, 559–575 (2021).

54. Gu, Y. J., Dziewonski, A. M., Su, W. & Ekström, G. Models of the mantle shear velocity and discontinuities in the pattern of lateral heterogeneities. *J. Geophys. Res. Solid Earth* **106**, 11169–11199 (2001).

55. Jackson, I. & Faul, U. H. Grain size-sensitive viscoelastic relaxation in olivine: Towards a robust laboratory-based model for seismological application. *Phys. Earth Planet. Inter.* **183**, 151–163 (2010).

56. Lau, H. C. & Faul, U. H. Anelasticity from seismic to tidal timescales: Theory and observations. *Earth Planet. Sci. Lett.* **508**, 18–29 (2019).

57. Connolly, J. A. Computation of phase equilibria by linear programming: a tool for geodynamic modeling and its application to subduction zone decarbonation. *Earth Planet. Sci. Lett.* **236**, 524–541 (2005).

58. Stixrude, L. & Lithgow-Bertelloni, C. Thermodynamics of mantle minerals -I. Physical properties. *Geophys. J. Int.* **162**, 610–632 (2005).

59. Stixrude, L. & Lithgow-Bertelloni, C. Thermodynamics of mantle minerals -II. Phase equilibria. *Geophys. J. Int.* **184**, 1180–1213 (2011).

60. Sun, S.-S. Chemical composition and origin of the Earth's primitive mantle. *Geochim. Cosmochim. Acta* **46**, 179–192 (1982).

61. Cobden, L., Goes, S., Cammarano, F. & Connolly, J. A. Thermochemical interpretation of one-dimensional seismic reference models for the upper mantle: evidence for bias due to heterogeneity. *Geophys. J. Int.* **175**, 627–648 (2008).

62. Houser, C., Hernlund, J., Valencia-Cardona, J. & Wentzcovitch, R. Discriminating lower mantle composition. *Phys. Earth Planet. Inter.* **308**, 106552 (2020).

63. Cobden, L. *et al.* Thermochemical interpretation of 1D seismic data for the lower mantle: The significance of nonadiabatic thermal gradients and compositional heterogeneity. *J. Geophys. Res. Solid Earth* **114** (2009).

64. Beyreuther, M. *et al.* Obspy: A Python toolbox for seismology. *Seismol. Res. Lett.* **81**, 530–533 (2010).

65. Schneider, S., Talavera-Soza, S., Jagt, L. & Deuss, A. FrosPy: Free oscillation Python toolbox for seismology. *Seismol. Res. Lett.* (2021).

66. Van Rossum, G. & Drake, F. L. *Python 3 Reference Manual* (CreateSpace, Scotts Valley, CA, 2009).

67. Wessel, P., Smith, W. H. F., Scharroo, R., Luis, J. & Wobbe, F. Generic mapping tools: improved version released. *Eos* **94**, 409–410 (2013).

68. Bird, P. An updated digital model of plate boundaries. *Geochem. Geophys. Geosyst.* **4** (2003).

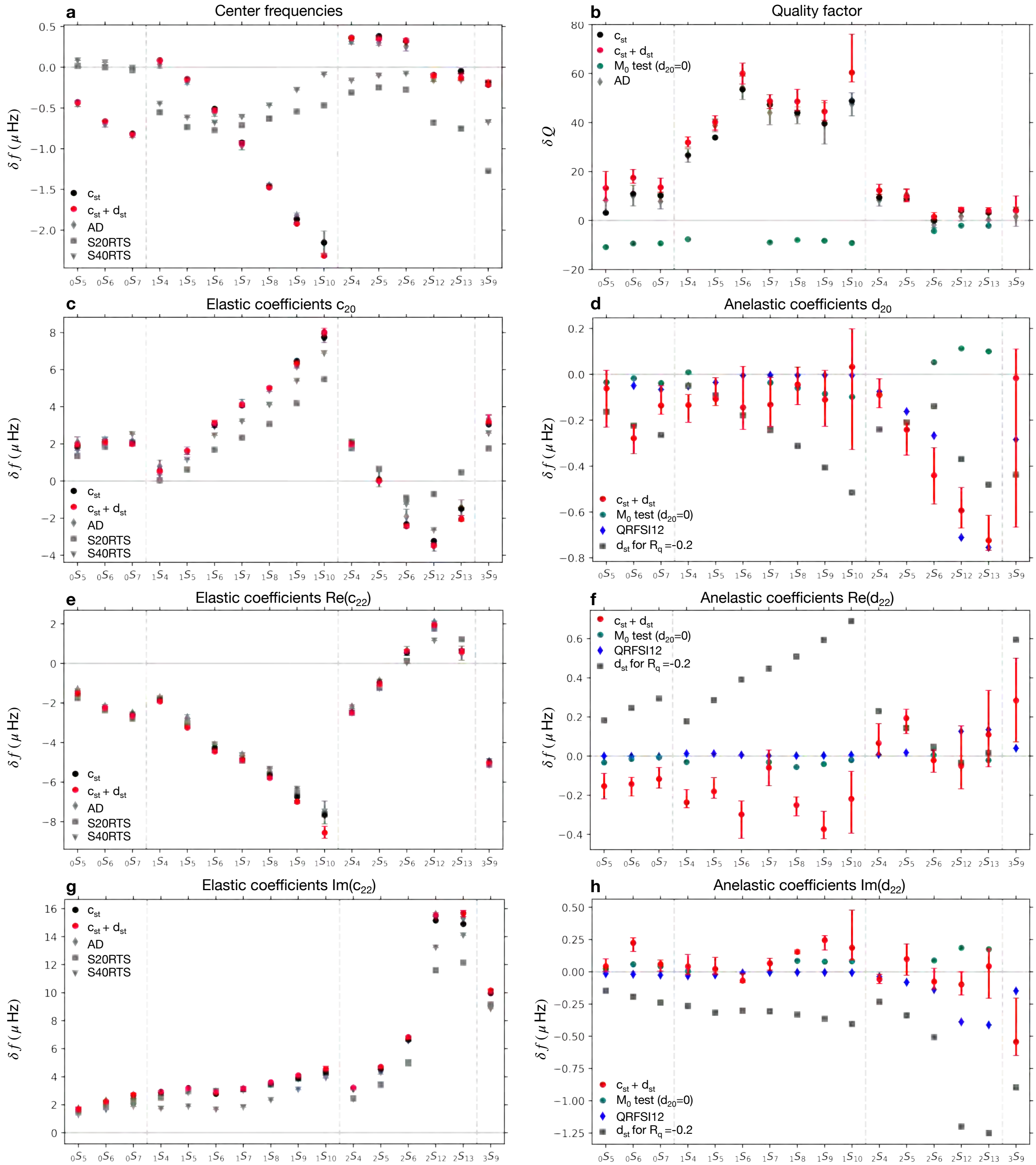

Extended Data Figure 1: **Splitting function coefficients measurements with respect to PREM (grey solid line)**. Only elastic splitting function observations (black); joint elastic and anelastic splitting function observations (red); joint splitting functions recovered from synthetic input structure containing only 3D v_s variations and scalar moment M_0 perturbations dependent on earthquake location (green). Elastic coefficients (a, c, e, g) are compared to previous measurements[18] and 3D v_s model predictions[46,50] (grey). Anelastic measurements (b, d, f, h) are compared to QRFSI12[3] predictions (blue); and a synthetic 3D Q_μ^{-1} global model obtained by scaling S20RTS[46] (grey).

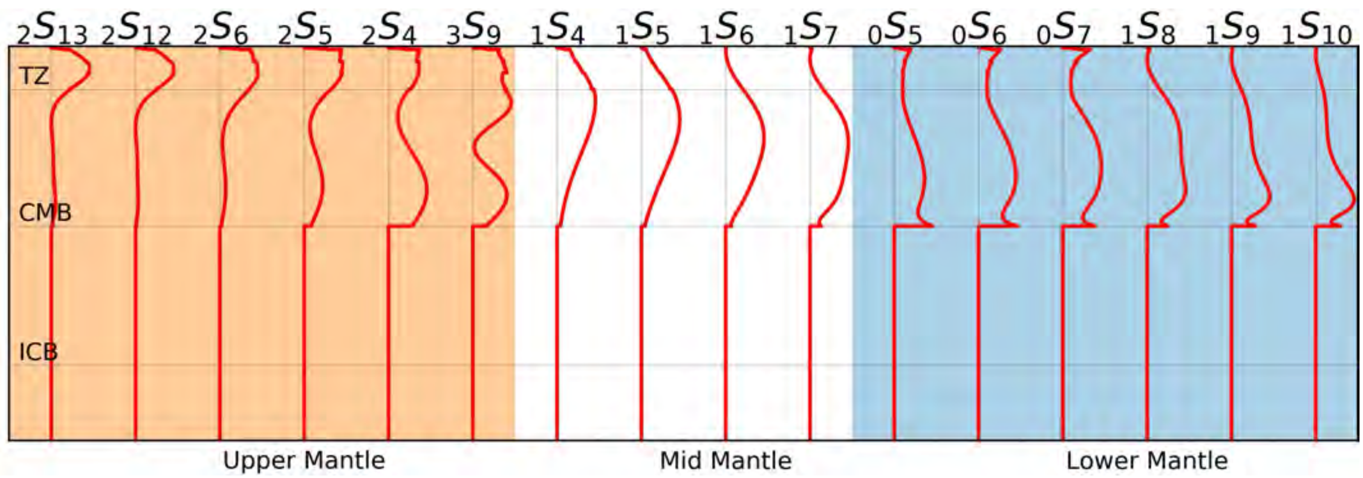

Extended Data Figure 2: **Sensitivity kernels**. Plotted as a function of depth for shear attenuation Q_μ^{-1} $(\mu_0 K_\mu)$, calculated for PREM. Modes are arranged and classified according to where they are most sensitive. The transition Zone (TZ), Core Mantle Boundary (CMB) and Inner Core Boundary (ICB) are marked in figure. All kernels are plotted for degree-zero.

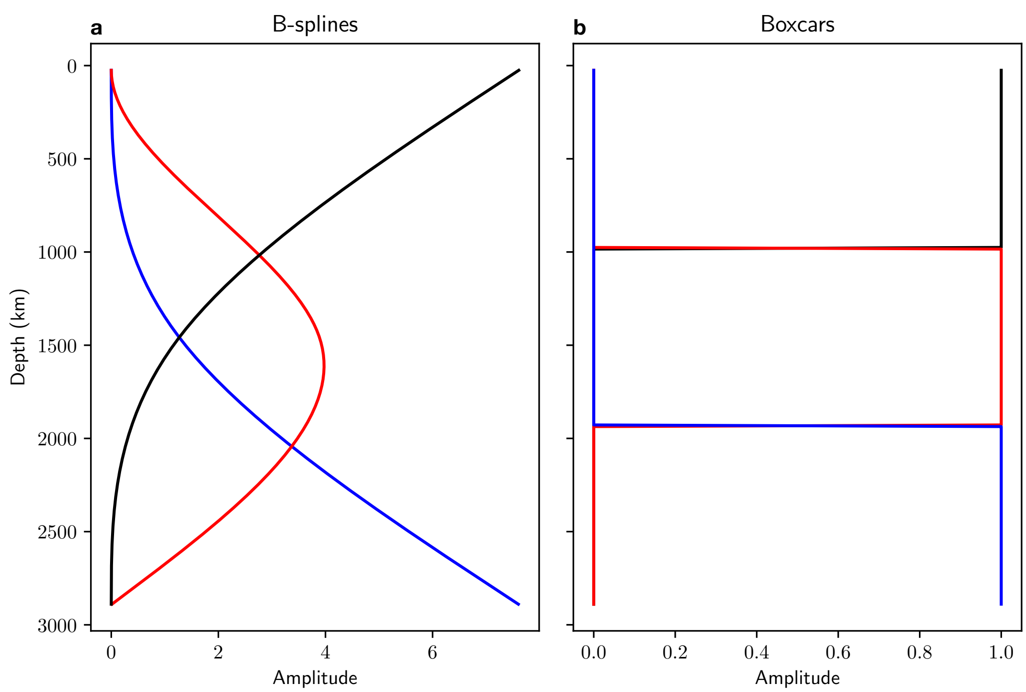

Extended Data Figure 3: **Depth parameterizations used in this study**. (a) B-splines and (b) boxcars.

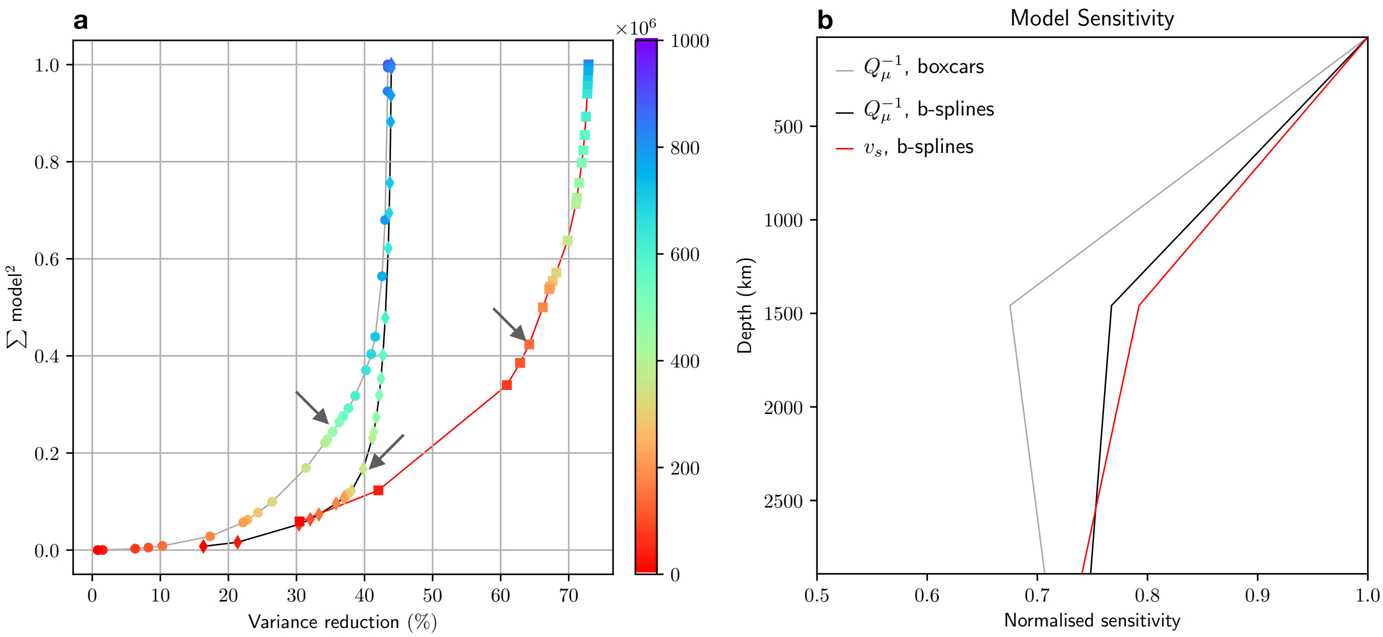

Extended Data Figure 4: **Model output**. (a) Model size versus variance reduction, the arrow points to the picked damping. The model size is normalized for an easier comparison. (b) Model sensitivity with depth using different depth parametrizations.

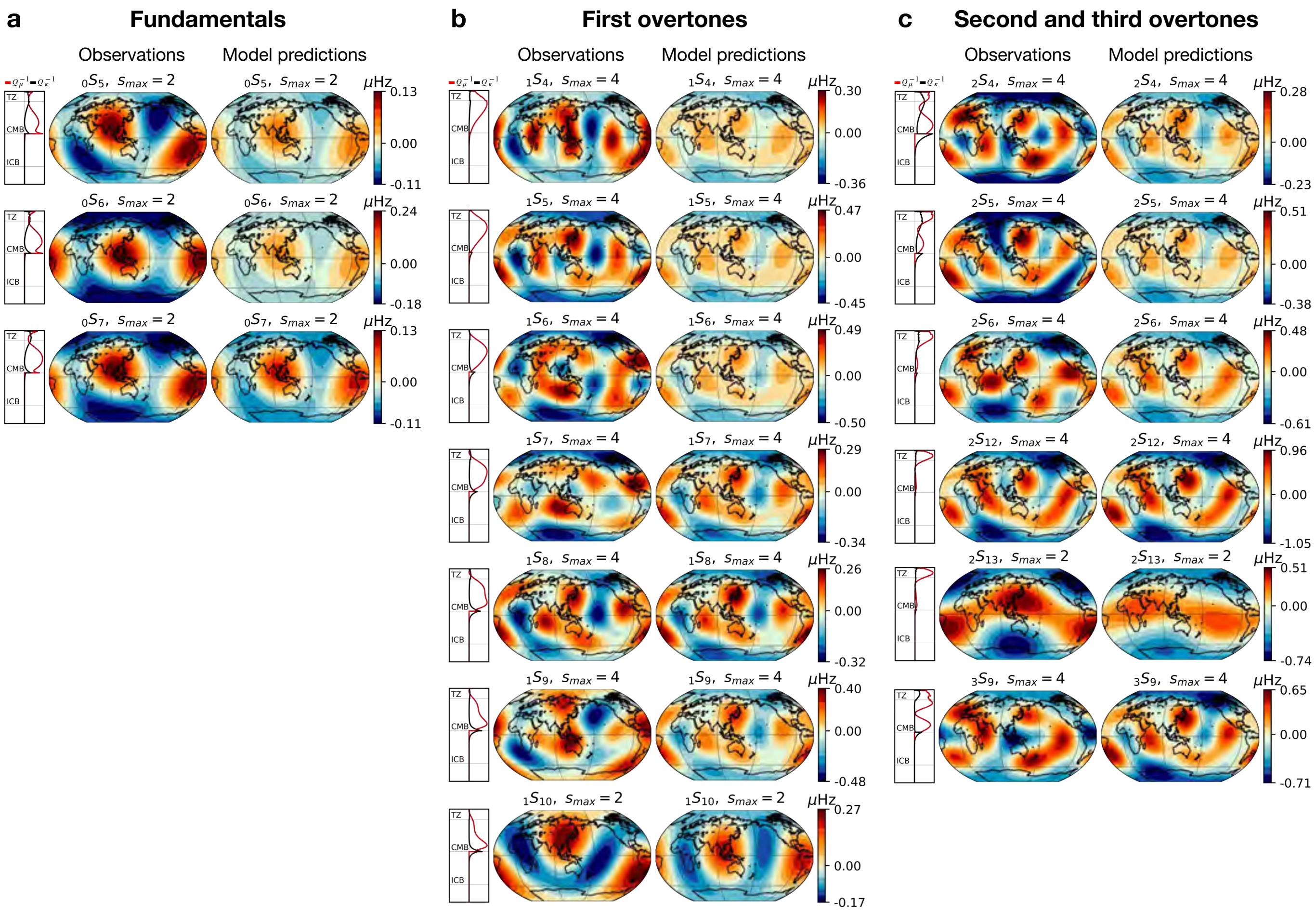

Extended Data Figure 5: **Observed anelastic splitting function maps compared to the anelastic predictions of our 3D Q_{μ}^{-1} model**. Plotted up to their maximum structural degree s_{max}, together with its sensitivity kernels for Q_{μ}^{-1} (red lines), and Q_{κ}^{-1} (black lines).

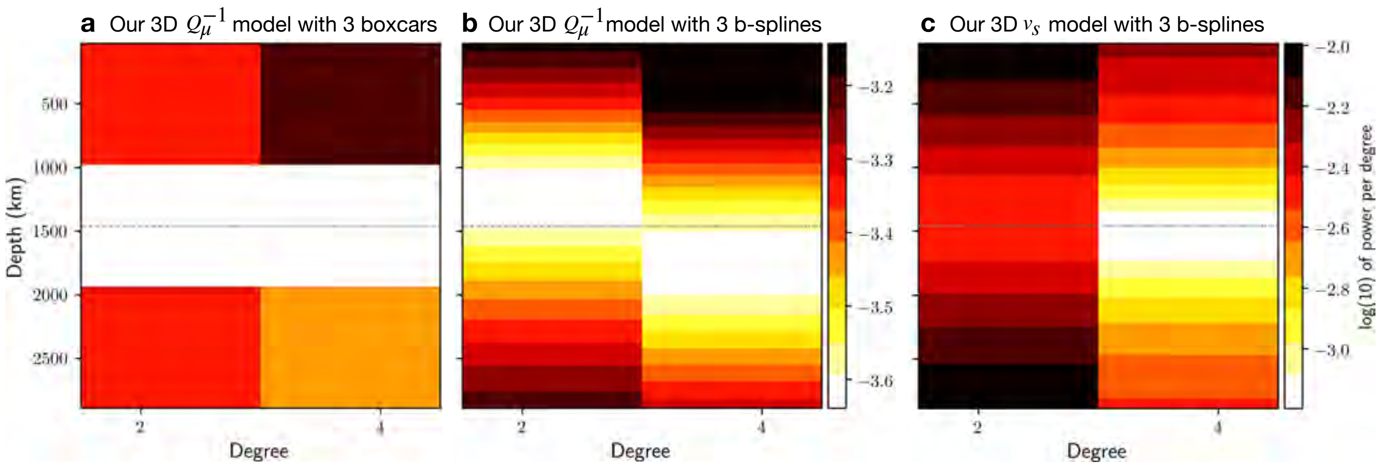

Extended Data Figure 6: **Spectral power of attenuation (a, b) and shear-wave velocity (c) heterogeneity per spherical harmonic degree**. The dashed grey line indicates the peak of our mid-mantle spline.

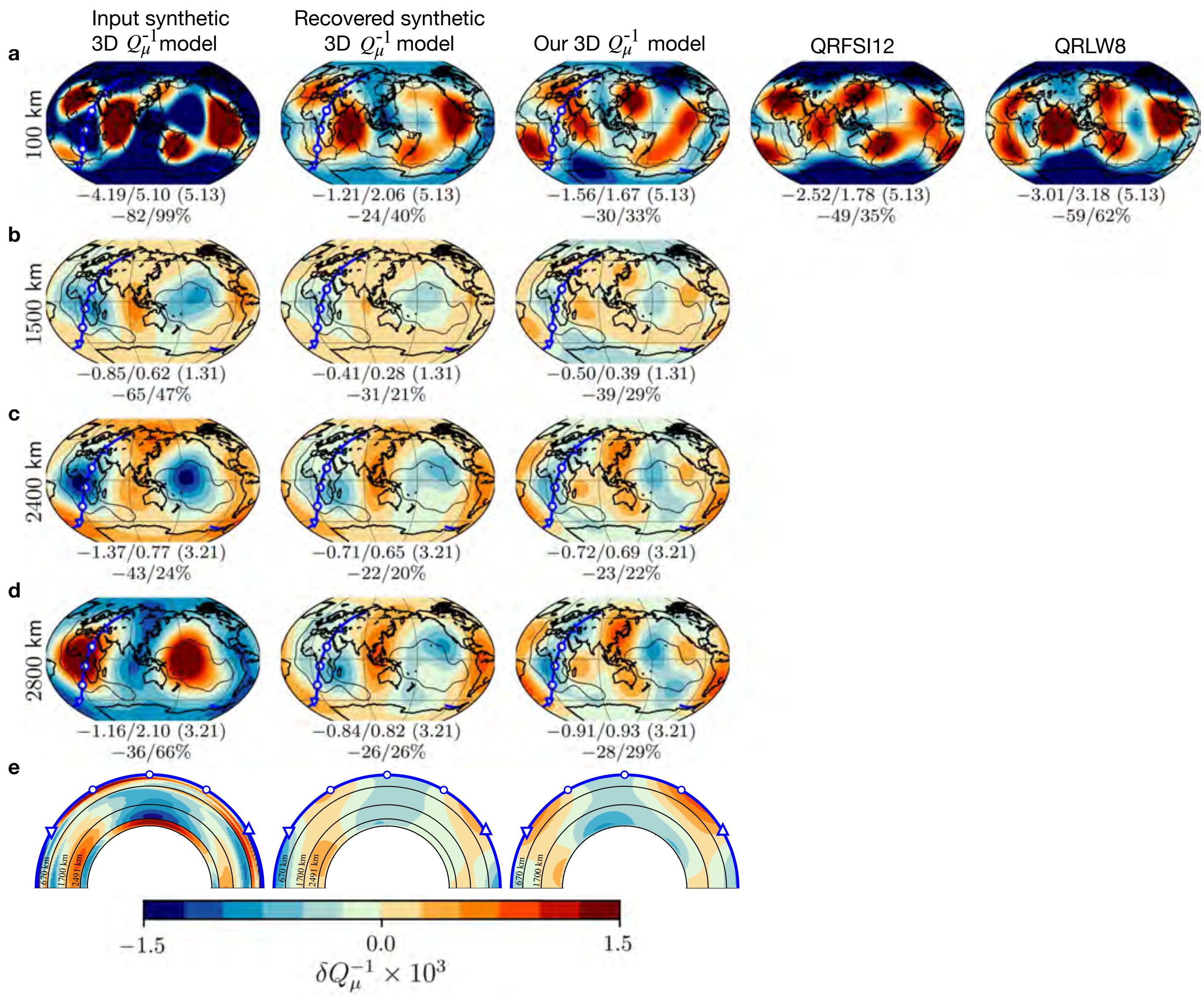

Extended Data Figure 7: **Comparison between our 3D Q_μ^{-1} synthetic input model (first column), our 3D Q_μ^{-1} synthetic recovered model (second column), and our 3D Q_μ^{-1} model (third column)**. For the (a) upper mantle, the tectonic plate boundaries[68] and the 3D upper mantle attenuation models QRLW8[2] and QRFSI12[3] are plotted. For the mid and lower mantle (b, c, d), the -0.1% v_s outline of the LLSVPs for tomographic model SP12RTS[21] at 2,850 km is included. A whole mantle cross-section for Africa (e) is shown. All models are plotted using even-degree structure for $s = 2, 4$. All attenuation models are plotted in terms of $\delta Q_\mu^{-1} \times 10^3$, which is presented as perturbation value and in percentage (with respect to PREM), together with the peak-to-peak value at each depth.

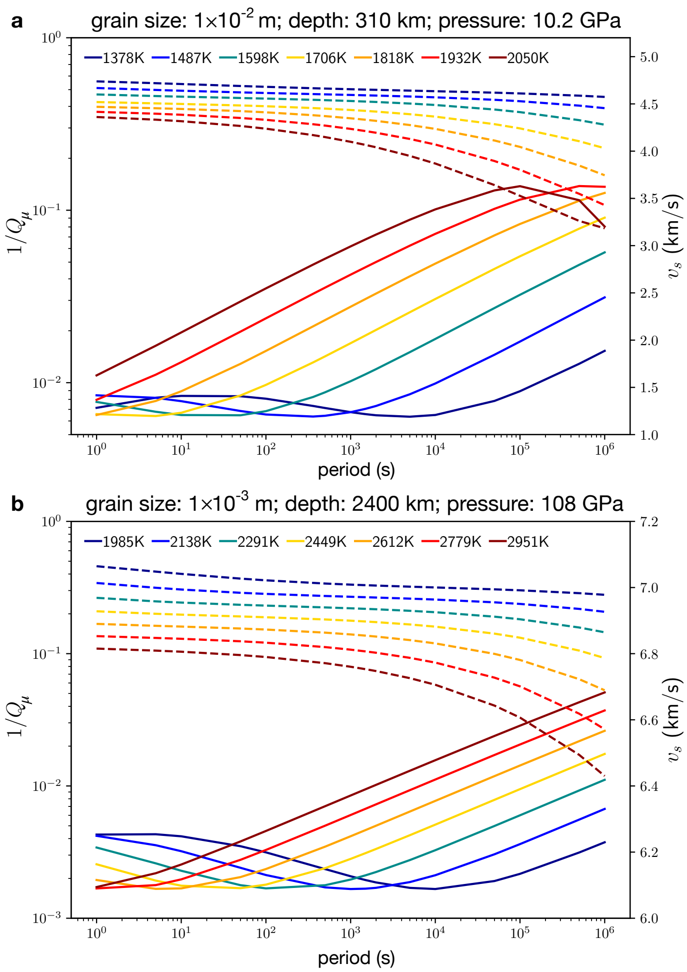

Extended Data Figure 8: **Relationship between attenuation ($1/Q_\mu$, solid lines) and shear velocity (v_s, dashed lines) and period**. Plotted or the (a) upper mantle and the (b) lower mantle. Temperature ranges were obtained using adiabats with potential temperatures (T_p) varying between 1273-1873 K.

Extended Data Table 1: **f_c (μHz) and Q measurements compared to PREM values (f_0, Q_0).** The s_{max} indicates the maximum structural order of the c_{st} and d_{st} observations in the $c_{st} + d_{st}$ scheme. Misfits are included for our measurements using only elastic splitting functions ($m^{c_{st}}$) and our measurements using both elastic and anelastic splitting functions ($m^{c_{st}+d_{st}}$). $\Delta m\%$ is the misfit reduction between $m^{c_{st}}$ and $m^{c_{st}+d_{st}}$. N_{ev} is the number of events, N_s is the number of stations used per seismic component.

	f_0	$f_c^{c_{st}}$	$f_c^{c_{st}+d_{st}}$	Q_0	$Q^{c_{st}}$	$Q^{c_{st}+d_{st}}$	s_{max}	$m^{c_{st}}$	$m^{c_{st}+d_{st}}$	$\Delta m\%$	N_{ev}^Z	N_s^Z	N_{ev}^R	N_s^R	N_{ev}^T	N_s^T
${}_0S_5$	840.42	839.99	$839.99^{+0.01}_{-0.01}$	356	359	369^{+7}_{-5}	8,2	0.083	0.080	3.4	74	763	4	19	4	17
${}_0S_6$	1038.21	1037.55	$1037.55^{+0.01}_{-0.004}$	347	358	365^{+3}_{-2}	10,2	0.111	0.108	3.1	92	1612	10	38	5	22
${}_0S_7$	1231.79	1230.98	$1230.96^{+0.01}_{-0.01}$	342	352	356^{+4}_{-2}	12,2	0.172	0.169	1.7	99	2207	21	104	18	81
${}_1S_4$	1172.85	1172.94	$1172.93^{+0.004}_{-0.004}$	271	298	303^{+2}_{-2}	6,4	0.160	0.158	1.2	87	1348	7	22	5	19
${}_1S_5$	1370.27	1370.13	$1370.12^{+0.01}_{-0.01}$	292	326	332^{+3}_{-3}	8,4	0.144	0.141	2.2	95	1880	27	196	27	148
${}_1S_6$	1522.04	1521.53	$1521.51^{+0.01}_{-0.02}$	346	399	406^{+4}_{-4}	8,4	0.152	0.148	3.0	93	1549	45	300	32	183
${}_1S_7$	1655.51	1654.59	$1654.57^{+0.02}_{-0.01}$	372	419	421^{+3}_{-3}	10,4	0.139	0.135	3.0	84	1520	0	0	0	0
${}_1S_8$	1799.30	1797.84	$1797.82^{+0.01}_{-0.01}$	380	424	428^{+5}_{-4}	12,4	0.130	0.127	2.1	84	1819	0	0	0	0
${}_1S_9$	1963.74	1961.87	$1961.82^{+0.01}_{-0.01}$	380	420	425^{+5}_{-4}	12,4	0.166	0.159	4.3	83	1356	0	0	0	0
${}_1S_{10}$	2148.42	2146.27	$2146.11^{+0.02}_{-0.01}$	378	427	439^{+16}_{-4}	12,2	0.258	0.250	3.3	78	868	0	0	0	0
${}_2S_4$	1379.20	1379.57	$1379.56^{+0.01}_{-0.01}$	380	390	393^{+2}_{-2}	6,6	0.144	0.141	2.2	95	1880	27	196	27	148
${}_2S_5$	1514.93	1515.31	$1515.28^{+0.01}_{-0.02}$	302	311	312^{+3}_{-2}	6,6	0.152	0.148	3.0	93	1549	45	300	32	183
${}_2S_6$	1680.84	1681.16	$1681.17^{+0.02}_{-0.03}$	238	238	239^{+2}_{-1}	10,6	0.158	0.152	3.4	95	1222	43	295	33	148
${}_2S_{12}$	2737.31	2737.22	$2737.21^{+0.02}_{-0.02}$	173	177	178^{+1}_{-1}	12,8	0.171	0.164	4.6	101	2734	14	32	15	27
${}_2S_{13}$	2899.90	2899.85	$2899.77^{+0.05}_{-0.02}$	174	178	178^{+1}_{-1}	12,2	0.355	0.345	2.7	101	1987	23	60	25	74
${}_3S_9$	2951.58	2951.39	$2951.36^{+0.06}_{-0.02}$	259	263	263^{+6}_{-1}	12,6	0.524	0.516	1.5	99	1997	40	210	29	140

Extended Data Table 2: **Parameters used in the anelastic scaling relationships of the Extended Burgers Model (EBM)[5,55]**

Parameters		Olivine	Bridgmanite + Periclase
Activation energy (kJ/mol)	E^*	375	286
Activation volume (m^3/mol)	V^*	6×10^{-6}	2×10^{-6}
Burgers element strength	Δ_B	1.04	2
Peak height	Δ_P	0.057	0.03
Anelastic frequency exponent	α	0.274	0.274
Viscous grain size exponent	m_M	3	3
Anelastic grain size exponents	m_H, m_L, m_P	1.31	1.31
Reference upper HTB[1] period (s)	τ_{HR}	10^7	10^{11}
Reference lower HTB[1] period (s)	τ_{LR}	10^{-3}	10^{-3}
Reference Maxwell period (s)	τ_{MR}	3.02×10^7	3.02×10^7
Reference peak period (s)	τ_{PR}	3.98×10^{-4}	3.98×10^{-4}
Peak width	σ	4	4
Reference temperature (°C)	T_R	900	900
Reference pressure (GPa)	P_R	0.2	0.2
Reference grain size (m)	d_R	13.4×10^{-6}	13.4×10^{-6}

[1] High Temperature Background (absorption band)

Supplementary Files

This is a list of supplementary files associated with this preprint. Click to download.

- dstSITCFD.pdf